Piecewise Small-Signal Modeling and Stability Analysis of DR-MMC HVDC System for Offshore Wind Farms via Floquet and Filippov Theory

Zefei Wu, Jianhang Zhu, *Member, IEEE*, Jiabing Hu, *Senior Member, IEEE*, Zeren Guo, *Student Member, IEEE*, Buyang Du, Yingbiao Li, *Member, IEEE*, and Jianbo Guo

***Abstract*—The diode rectifier (DR) modular multilevel converter (MMC) high-voltage direct current (HVDC) has generated increasing interest in connecting deep-sea offshore wind farms. To evaluate the system stability, this article introduces the Filippov theory to describe the system behavior during the switching of DR, which is the key to accurately modeling the DR-MMC HVDC system. Given that the obtained small-signal model is piecewise and time-varying, combining it with Floquet theory enables a comprehensive analysis of system stability. Compared to the existing model, the proposed model fully incorporates the switching dynamics and commutation process of DR, offering a precise depiction of the system's stability range as parameters vary. In contrast, the existing model tends to yield inaccurate stability analysis results. The correctness of stability analysis results is verified by electromagnetic transient tests from RT-LAB.**

***Index Terms*—Diode rectifier (DR), Filippov, Floquet, modular multilevel converter (MMC), stability analysis.**

NOMENCLATURE

L_{t_mmc}, T_{MMC}	Leakage inductance and turn ratio of MMC transformer.
L_{arm}, R_{arm}	Inductance and resistance of MMC arm.
C_{arm}	Equivalent capacitance of MMC arm.
L_r, T_{DR}	Leakage inductance and turn ratio of DR transformer.
L_{t_vsc}, R_{t_vsc}	Inductance and resistance of WT.
T_{vsc}	Transformer ratio of WT.
$C_{\mathrm{dc\_vsc}}$	DC-link capacitance of WT.
L_d, R_d	DC-link inductance and resistance of DR-MMC.
L_{ac}, R_{ac}, C_{ac}	AC line inductance, resistance, and capacitance.
ω_c, a_f	Bandwidth of LPF.
i_{MMC}, i_{DR}, i_{vsc}	Primary currents of MMC, DR and WT.
i_{dc}, u_{dc}	DC-link current and voltage of DR-MMC.
I_{in}, $u_{\mathrm{dc\_vsc}}$	DC-link current and voltage of WT.
$\boldsymbol{u}_t$	Terminal voltage of WT.
$\boldsymbol{u}_{pcc}$	Terminal voltage of PCC.
$u_{j\_\mathrm{mmc}}, i_{j\_\mathrm{mmc}}$ $(j = a, b, c)$	Voltage and current in ac sider of MMC.
u_{j1}, u_{j2}	Voltages in ac side of DR with star-star and star-delta connections.
i_{j1}, i_{j2}	Currents in ac side of DR with star-star and star-delta connections.

Superscript

Δ	Differential-mode component (DMC).
Σ	Common-mode component (CMC).
u, l	Variables of upper arm and lower arm.
$*$	Reference value.

Subscript

d, q	Direct- and quadrature-axis components in dq rotating coordinate.
$+, -$	Positive and negative components.

Received 25 March 2025; accepted 20 May 2025. Date of publication 28 May 2025; date of current version 5 August 2025. This work was supported by the National Natural Science Foundation of China under Grant U22B20122 and Grant U23B20120. Recommended for publication by Associate Editor Z. Qin. *(Corresponding author: Jianhang Zhu.)*

Zefei Wu, Jiabing Hu, Zeren Guo, Buyang Du, and Yingbiao Li are with the State Key Laboratory of Advanced Electromagnetic Technology, School of Electrical and Electronic Engineering, Huazhong University of Science and Technology, Wuhan 430074, China (e-mail: zefei_wu@hust.edu.cn; j.hu@mail.hust.edu.cn; zeren98@hust.edu.cn; buyang_du@hust.edu.cn; liyb@hust.edu.cn).

Jianhang Zhu is with the Department of Electrical and Electronic Engineering, University of Hong Kong, Hong Kong 999077, SAR, China, and also with the Shenzhen Institute of Research and Innovation, University of Hong Kong, Shenzhen 518057, China (e-mail: jianhang@hku.hk).

Jianbo Guo is with China Electric Power Research Institute, Beijing 100192, China (e-mail: guojb@epri.sgcc.com.cn).

Color versions of one or more figures in this article are available at https://doi.org/10.1109/TPEL.2025.3574469.

Digital Object Identifier 10.1109/TPEL.2025.3574469

I. INTRODUCTION

RECENTLY, deep-sea offshore wind farms (OWFs) have experienced rapid development due to greater wind speed and proximity to the load center. In comparison to high-voltage alternating current transmission, high-voltage direct current (HVDC) transmission has emerged as the preferred solution for large-capacity, long-distance delivery of OWF, owing to its lower power loss and reduced costs [1], [2]. The modular multilevel converter (MMC) based HVDC is widely utilized in practical engineering due to its flexible control capabilities and modular structure [3], [4].

However, constrained by the size limitations of offshore converter platforms and economic considerations, [5] proposed the use of a diode rectifier (DR) based HVDC system for OWFs.

Compared to MMCs, DR offers a smaller volume, lower price, and reduced power loss. Nonetheless, this topology relies on external ac voltage and frequency support to maintain stable operation. To address this issue, various hybrid configurations combining DR and MMC have been proposed, including parallel [6], series configurations [7], and so on. The series topology, in particular, facilitates the sharing of dc voltage between DRs and MMC, thereby reducing the voltage stress requirements. The advantages of the DR-MMC topology have generated increasing interest and exhibit significant potential for further development [8], [9].

Despite the promising prospects of the DR-MMC HVDC system for OWFs, ensuring their safe and stable operation remains a primary concern [9]. Here, we focus on the small-signal dynamic stability. Although significant advancements have been made in the small-signal modeling and stability analysis of MMC [10], [11], [12], [13], the corresponding work for DR-MMC HVDC systems remains relatively nascent. The main challenges arise from the complex frequency coupling between DR and MMC, as well as the switching dynamics and commutation process of DR [9], [14]. Since diodes are uncontrolled devices, they can only switch at the natural commutation point [15], and the switching frequency is comparable to the power grid frequency. The periodic switching of diodes induces constant changes in circuit structure, resulting in a system with non-differentiable points and abundant characteristic harmonics, primarily concentrated around several hundred Hz [16]. Therefore, the switching dynamics of DR play a critical role in the system's broadband stability. To accurately evaluate its stability, relevant methods have garnered increasing research interest.

The state-space averaging method was widely introduced for the stability analysis of switching circuits with periodic trajectories [17]. It provides a simple and effective model for stability analysis at timescales much slower than the switching cycle. However, for systems operating at low switching frequencies, such as DR, this approach fails to capture the strong effects of switching behavior on stability [18]. To address this, one approach involves the use of the Poincaré map. The periodic trajectories of switching circuits correspond to fixed points on the Poincaré map, and the stability of these trajectories can be deduced from the Jacobian matrix at the fixed points [19]. The intrinsic theoretical rigor of this method ensures accurate analysis results. However, its derivation is cumbersome and cannot be directly applied in DR-MMC, because the map cannot be obtained in closed form [18]. Alternatively, the switching dynamics can be described by introducing switching functions. By performing a Fourier series expansion of the switching functions, nondifferentiable points can be smoothed, making the functions differentiable. Based on this approach, the impedance model of DR is built [20], which also has been improved after considering the frequency coupling and multiharmonics [9], [21]. However, these works primarily focus on the dynamics of low-order components (up to three-order), while the neglected higher-order components, such as the characteristic harmonics of DR, have important effects on the system stability [22]. Through the harmonic transfer function concept [23], it can also be extended to any required frequency. Nevertheless, when considering the commutation process of DR in detail, the switching functions include a commutation overlap angle, which is implicitly embedded in the differential equation of the voltage-current relationship [14]. To explicitly derive the commutation overlap angle, existing methods typically assume a constant current on the dc side and a sinusoidal voltage on the ac side [9]. These assumptions degrade the modeling accuracy.

The piecewise modeling method based on the characteristics of switching circuits presents a potential solution. [24] developed a piecewise model for a single-phase bridge DR circuit based on its operational characteristics. By using this approach, there is no need for switching functions to describe the voltage-current relationship on the ac and dc sides, thereby avoiding the introduction of the assumptions to calculate the commutation overlap angle. However, it simplifies the overall piecewise small-signal model to a mere combination of each interval, neglecting the system's behavior during switching, which is the key to describing such systems [18]. To address this, Filippov's theory [25] is previously introduced into the stability analysis of some simple power electronic circuits [18], such as a buck dc/dc converter. However, few publications involved the study of piecewise modeling considering Filippov's theory in DR systems, let alone DR-MMC HVDC.

To overcome the above-mentioned issues and achieve higher model accuracy, a piecewise small-signal model of DR-MMC HVDC for OWFs is established in this article using Filippov's theory. By calculating the saltation matrix at switching instant, the system's behavior during switching is accurately captured. Consequently, the overall piecewise small-signal model is composed of the small-signal models for each interval, combined with the saltation matrix at switching instant. Since the proposed model is periodic, combining it with Floquet theory ensures the accuracy of small-signal stability analysis [11].

The main contributions of this article are summarized as follows:

1) The proposed model accounts for all characteristic harmonics related to the switching dynamics of DR, leading to higher accuracy.
2) There is no need to use switching functions, eliminating the assumptions required for calculating the commutation overlap angle [9], [14], thereby accurately reflecting the commutation process.
3) Although Filippov's theory has been applied to simple power electronic circuits, like dc/dc converters [18], [25], this article contains the first application of this theory to such a complex ac/dc system, i.e., DR-MMC HVDC.

Compared with the proposed model, the existing model [9] either neglects the characteristic harmonics of DR or relies on assumptions for calculating the commutation overlap angle, tending to yield inaccurate stability boundaries as parameters vary.

The rest of this article is organized as follows. Section II illustrates the topology and builds the original mathematical model of the DR-MMC HVDC system. Then, the piecewise small-signal model is constructed and verified in Section III. In Section IV, the system's stability is analyzed using the eigenvalue analysis method. Section V verifies the stability analysis

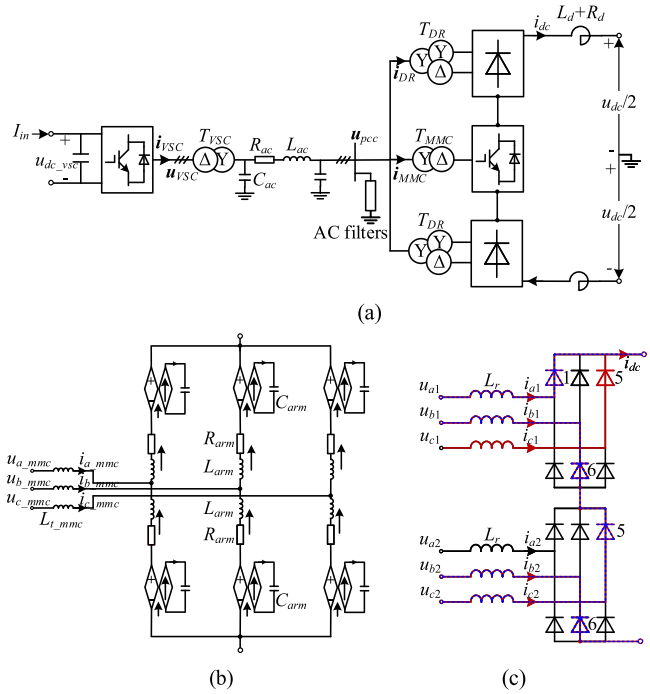

Fig. 1. Configuration of (a) DR-MMC HVDC system, (b) MMC, and (c) 12-pulse DR.

results by electromagnetic transient tests from RT-LAB. Finally, Section VI concludes this article.

II. Studied System and Its Original Math Model

A. System Configuration and Its Control

The configuration of DR-MMC HVDC for OWFs is shown in Fig. 1(a). The OWFs are modeled as an aggregated type-4 wind turbine (WT), with the generator side dynamics neglected due to their little impact on the grid side dynamics [26]. The DR-MMC HVDC consists of two 12-pulse DRs, and an MMC, which are connected in parallel on the ac side and series on the dc side. Both 12-pulse DRs have the same circuit structure and parameters. The configurations of MMC and 12-pulse DR are shown in Fig. 1(b) and (c). Each 12-pulse DR consists of two 6-pulse DRs with a 30° phase shift achieved through different transformer connections. The ac filters are configured at the point of common coupling (PCC) to eliminate the 11th and 13th harmonics, and its structure refers to [9]. Since the equivalent switching frequencies of WT and MMC are high, their discrete switching processes are averaged, which is sufficient for capturing dynamics below half of the switching frequency [27]. However, for DR, since the diode switching frequency is comparable to the power grid frequency, its switching behaviors are explicitly considered due to their significant impact on system stability.

The control structures of MMC and WT are shown in Fig. 2. MMC operates in grid-forming mode to establish the offshore ac network, incorporating positive/negative sequence terminal voltage control (PSTVC/NSTVC), positive/negative sequence differential-mode component (DMC) current control (PSDMC/NSDMC), circulating current suppression control

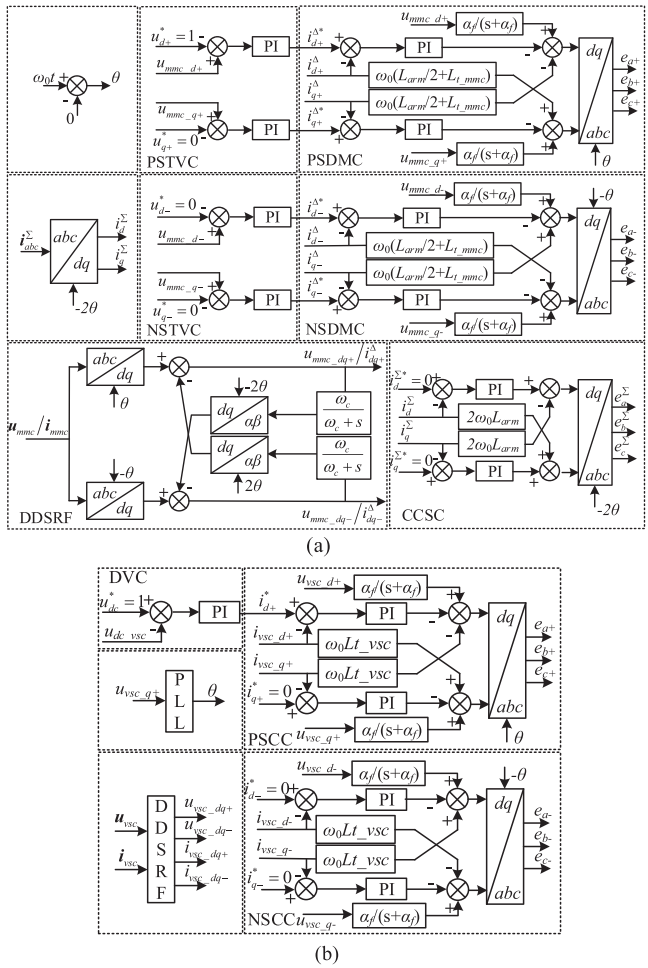

Fig. 2. Control structure of (a) MMC and (b) WT.

(CCSC) [11]. All these control variables come from the decoupled double synchronous reference frame (DDSRF) control [11]. The WT achieves synchronization by tracking the phase angle of terminal voltage using a phase-locked loop (PLL). Its control structure includes dc-link voltage control (DVC), positive/negative sequence current control, and DDSRF-PLL.

B. Original Math Model of the Studied System

The studied system can be divided into four parts: DR-MMC converter; WT; ac network; and control systems. Since the last three parts are all continuous after averaging, and their modeling has been extensively studied in previous works [11], [29], this article will not elaborate on these aspects and focus on the piecewise modeling of the DR-MMC converter.

During normal operation, the 12-pulse DR's noncommutation process (four valves) and commutation process (five valves) conduct alternately within each 1/12th of a cycle. This divides a fundamental frequency period into 24 intervals, including 12 noncommutation processes and 12 commutation processes. Then, take one of these intervals as an example, we focus on the VT156/VT56 conduction, as indicated by the red solid line in Fig. 1(c).

The upper and lower arm currents of MMC $i_j^{u/l}$ (where $j = a, b, c$) contain dc and ac components. According to [11], these can be expressed as a combination of DMC and common-mode component (CMC)

$$i_j^u = i_j^\Sigma + \tfrac{1}{2} i_j^\Delta \;\vdots\; i_j^l = i_j^\Sigma - \tfrac{1}{2} i_j^\Delta \tag{1}$$

where DMC current i_j^Δ corresponds to the ac grid current, forming the input current of MMC, and i_j^Σ is the CMC current, which flows through the entire phase leg.

Since the transformer of MMC is typically star-delta connected, it is assumed that there is no dc bias and even harmonics on the ac side. This implies that the sum of the three-phase DMC currents is zero, which can be expressed as

$$\sum_{x=a,b,c} i_x^\Delta = 0. \tag{2}$$

Therefore, the current on the dc side i_{dc} can be expressed as the sum of the three-phase CMC currents

$$i_{\mathrm{dc}} = \sum_{x=a,b,c} i_x^\Sigma. \tag{3}$$

In addition, the dynamics of the two 12-pulse DRs are consistent due to the same ac voltage. The voltage equations for the upper and lower arms of the DR-MMC can be derived using Kirchhoff's voltage law (KVL), and they can be decomposed into two parts: one related to DR and the other related to MMC. Besides, the arm voltages for the upper and lower arms $u_{mj}^{u/l}$ also contain DMC and CMC. They can be expressed as

$$u_{mj}^\Sigma = \tfrac{1}{2}\left(u_{mj}^u + u_{mj}^l\right) \;\vdots\; u_{mj}^\Delta = -\tfrac{1}{2}\left(u_{mj}^u - u_{mj}^l\right). \tag{4}$$

Then, the dynamics of the ac and dc side can be initially separated as follows:

$$-u_{j\_\mathrm{mmc}} + \left(L_{t\_\mathrm{mmc}} + \frac{L_{\mathrm{arm}}}{2}\right)\frac{di_j^\Delta}{dt} + \frac{R_{\mathrm{arm}}}{2} i_j^\Delta + u_{mj}^\Delta = 0 \tag{5}$$

$$\begin{pmatrix} -u_{a1} + u_{b2} - u_{c2} + u_{b1} + \\ L_r \frac{di_{a1}}{dt} + (L_d + 3L_r) \cdot \sum_{x=a,b,c} \frac{di_x^\Sigma}{dt} + R_d \sum_{x=a,b,c} i_x^\Sigma \end{pmatrix} + \frac{u_{dc}}{2} + \left(L_{arm}\frac{di_j^\Sigma}{dt} + R_{arm} i_j^\Sigma - u_{mj}^\Sigma\right) = 0. \tag{6}$$

In addition, during the commutation process, the simultaneously conducted valves VT1 and VT5 form a closed circuit, short-circuiting the phase-A and the phase-C of the upper six-pulse DR. The corresponding voltage equation can be expressed as

$$-u_{c1} + L_r \cdot \left(\sum_{x=a,b,c} \frac{di_x^\Sigma}{dt} - \frac{di_{a1}}{dt}\right) - \left(-u_{a1} + L_r \frac{di_{a1}}{dt}\right) = 0. \tag{7}$$

Therefore, (5)–(7) describe the main dynamics of the DR-MMC converter during the VT156/VT56 conduction period. The dynamics of the submodules capacitance-voltage of MMC are not elaborated here, as they have been comprehensively detailed in [11]. It is evident that the ac side dynamics represented by (5) are independent of DR and thus remain the same throughout the entire period. Conversely, the dc side dynamics described by (6) and the dynamic of the commutation process represented by (7) are dependent on DR. Therefore, these dynamics vary across different intervals and require individual modeling for each one. The equations for the remaining 23 intervals can be readily derived using the same approach. It should be noted that when the commutation process ends and VT16/VT56 conducts [as shown by the blue dashed line in Fig. 1(c)], the commutation-related (7) disappears. This indicates that the state space dimension changes when the diodes switch [19].

Combining the dynamics of WT, ac network, and control systems, the DR-MMC HVDC system can be expressed as:

$$\begin{cases} \dot{\boldsymbol{x}}_p = \boldsymbol{f}_{pi}, t_{i-1} < t < t_i \\ \dot{\boldsymbol{x}}_o = \boldsymbol{f}_o \end{cases} \tag{8}$$

where $\boldsymbol{x}_p = [\boldsymbol{i}_{j1}\, \boldsymbol{i}_{j2}\, \boldsymbol{i}_j^\Sigma]^T$, are the state variables associated with switching, and $\boldsymbol{f}_{pi}$ (for $i = 1, \ldots, 24$) represents the differential equations corresponding to each interval, with t_i indicating the time of the switching instant. $\boldsymbol{x}_o$ are continuous dynamics state variables and its corresponding differential equations are $\boldsymbol{f}_o$. It should be noted that redundant state variables are included in $\boldsymbol{x}_p$ for stability analysis purposes. While (8) provides a general mathematical model of the system, the detailed derivation results for $\boldsymbol{x}_p$ in each interval are presented in Appendix A.

The system incorporates both continuous-time dynamics and discrete-event dynamics, and is generically categorized as a hybrid system [30]. It is referred to as a piecewise model to emphasize its key characteristics. Switching events make parts of the system toggle between multiple sets of differential equations [18]. The complex dynamical behavior of such a hybrid system presents significant challenges for small-signal modeling and stability analysis.

III. Small-Signal Modeling of the Studied System

Since the original mathematical model is nonlinear and piecewise smooth, two different methods are employed in this section to derive the small-signal models for each smooth interval and at the switching instants, respectively.

A. Small-Signal Modeling for Each Smooth Interval

For a smooth system, its nonlinear mathematical model can be represented by a set of differential equations

$$\dot{\boldsymbol{x}} = \boldsymbol{f}(\boldsymbol{x}, t). \tag{9}$$

Smoothness implies that $\boldsymbol{f}$ is differentiable everywhere in a given domain. If (9) has a solution with period T, its small-signal model can be built by linearizing the system around the whole periodic orbit [11]

$$\Delta\dot{\boldsymbol{x}}(t) = \boldsymbol{J}(t) \cdot \Delta\boldsymbol{x}(t), \boldsymbol{J}(t) = \left.\frac{\partial \boldsymbol{f}}{\partial \boldsymbol{x}}\right|_{\boldsymbol{x}_{ss}} \tag{10}$$

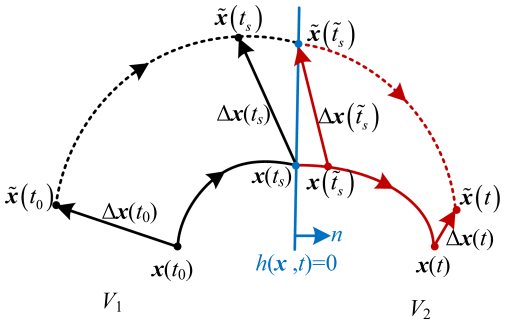

Fig. 3. Trajectory of piecewise smooth system and its perturbed trajectory.

where $\boldsymbol{J}$ is the Jacobian matrix of $\boldsymbol{f}$, representing the partial derivative of $\boldsymbol{f}$ concerning $\boldsymbol{x}$, and $\boldsymbol{x}_{ss}$ is the periodic solution of the system.

Therefore, for the studied system, by neglecting switching instants and linearizing the system around the periodic trajectory, the small-signal model in each interval can be expressed as

$$\begin{cases} \Delta\dot{\boldsymbol{x}}_p = \boldsymbol{J}_{pi}\Delta\boldsymbol{x}_p, t_{i-1} < t < t_i \\ \Delta\dot{\boldsymbol{x}}_o = \boldsymbol{J}_o\Delta\boldsymbol{x}_o \end{cases} \tag{11}$$

where $i = 1, \ldots, 24$, $\boldsymbol{J}_{pi}$ is the Jacobian matrix of $\boldsymbol{f}_{pi}$, $\boldsymbol{J}_o$ is the Jacobian matrix of $\boldsymbol{f}_o$, both derived using the Symbolic Math Toolbox in MATLAB.

B. Small-Signal Modeling at Switching Instants

1) Filippov's Method: Since the studied system is nondifferentiable at switching instants, one approach is to ignore these non-differentiable points, as done in [24]. However, this would result in the loss of switching dynamics. To develop a complete small-signal model over the entire period, Filippov's method was employed [18], [25], [31]. This method effectively handles the non-smooth dynamics inherent in such systems. While comprehensive details of Filippov's method are available in the above literature, a brief overview is provided here.

For a power system with switching behavior, the state is typically continuous but non-smooth, and can be represented as a piecewise function:

$$\dot{x} = \begin{cases} \boldsymbol{f}_1(\boldsymbol{x}, t), x \in V_1 \\ \boldsymbol{f}_2(\boldsymbol{x}, t), x \in V_2 \end{cases} \tag{12}$$

where V_1 and V_2 are two different regions in state space.

The transition between the two sets of differential equations f_1 and f_2 is determined by a switching event, which occurs when the following scalar function holds:

$$h(\boldsymbol{x}, t) = 0. \tag{13}$$

The system's dynamic behavior and the small perturbation behavior around the periodic orbit are shown in Fig. 3. The original trajectory of the system is represented by the solid line, crossing the switching boundary at time t_s. When a perturbation $\Delta\boldsymbol{x}(t_0)$ is applied at the initial time t_0, the resulting perturbed trajectory is indicated by the dashed line, which crosses the switching boundary at the time $\tilde{t}_s$. This illustrates that the

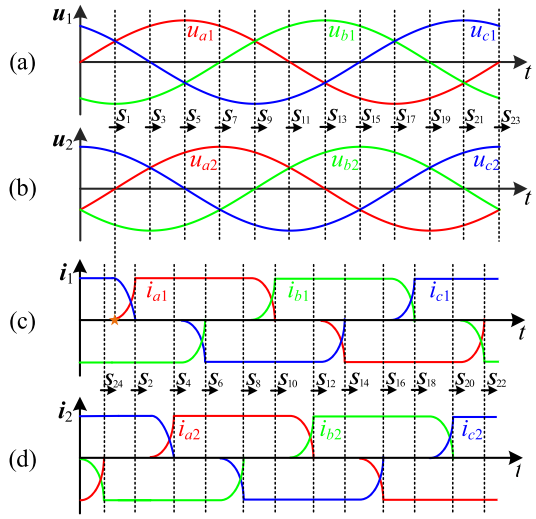

Fig. 4. Ideal waveforms of starstar transformer voltage (a) and current (c), stardelta transformer voltage (b) and current (d) of the DR.

times at which the original and perturbed trajectories reach the switching boundary differ, leading to an abrupt change in $\Delta\boldsymbol{x}(t)$ at the switching instant. The $\Delta\boldsymbol{x}(t_s)$ and $\Delta\boldsymbol{x}(\tilde{t}_s)$ before and after the switching can be related by a map $\boldsymbol{S}$, which is called the saltation matrix [18]

$$\boldsymbol{S} = \boldsymbol{I} + \frac{(\boldsymbol{f}_2(\boldsymbol{x}(t_s), t_s) - \boldsymbol{f}_1(\boldsymbol{x}(t_s), t_s)) \cdot \boldsymbol{n}^T}{\boldsymbol{n}^T \cdot \boldsymbol{f}_1(\boldsymbol{x}(t_s), t_s) + \boldsymbol{m}} \tag{14}$$

where $\boldsymbol{I}$ is the identify matrix, $\boldsymbol{n} = \frac{\partial h}{\partial \boldsymbol{x}}|_{(\boldsymbol{x}(t_s), t_s)}$ and $\boldsymbol{m} = \frac{\partial h}{\partial t}|_{(\boldsymbol{x}(t_s), t_s)}$.

2) Derivation of Saltation Matrix for the Studied System: To take into account the abrupt changes in the studied system at the switching instants, the corresponding saltation matrices need to be derived. In this article, two types of switching events are defined to describe the switching of DR. The first type of switching event describes the transition from the noncommutation process to the commutation process. As illustrated in Fig. 4(a) and (b), the switching of diodes is uncontrolled and dependent on the grid voltage. The corresponding scalar function can be expressed as

$$h_{2i-1}(x, t) = u_{pp} = \begin{cases} u_{a1} - u_{c1}, i = 1, 7 \\ u_{a2} - u_{c2}, i = 2, 8 \\ u_{b1} - u_{c1}, i = 3, 9 \\ u_{b2} - u_{c2}, i = 4, 10 \\ u_{b1} - u_{a1}, i = 5, 11 \\ u_{b2} - u_{a2}, i = 6, 12 \end{cases} \tag{15}$$

where u_{pp} denotes the phase-to-phase voltage, and the first type of switching event occurs when the phase-to-phase voltage crosses zero.

Therefore, the saltation matrix resulting from the first type of switching event can be expressed as

$$\boldsymbol{S}_{2i-1} = \boldsymbol{I} +$$

$$\frac{\left(\boldsymbol{f}_{2i-1}\left(\boldsymbol{x}\left(t_{2i-2}\right),t_{2i-2}\right)-\boldsymbol{f}_{2i-2}\left(\boldsymbol{x}\left(t_{2i-2}\right),t_{2i-2}\right)\right)\cdot\left(\frac{\partial u_{pp}}{\partial \boldsymbol{x}}\right)^{T}}{\left(\frac{\partial u_{pp}}{\partial \boldsymbol{x}}\right)^{T}\cdot\boldsymbol{f}_{2i-2}\left(\boldsymbol{x}\left(t_{2i-2}\right),t_{2i-2}\right)} \tag{16}$$

where $i=1,\ \ldots,12$, $\boldsymbol{f}_{2i\text{-}1}=[\boldsymbol{f}_{p2i\text{-}1}\ \boldsymbol{f}_o]^T$ is a simplified expression for an interval in (8). When $2i\text{-}2=0$, $\boldsymbol{f}_{2i\text{-}2}=\boldsymbol{f}_{24}$.

The second type of switching event describes the transition from the commutation process to the non-commutation process. This can be calculated by combining $t_{2i\text{-}2}$ with the commutation overlap angle, and the corresponding scalar function can be expressed as

$$h_{2i}\left(x,t\right)=t_{2i-2}+T\mu_i/2\pi-t \tag{17}$$

where μ_i is the commutation overlap angle for the 12 diodes.

Typically, under the assumptions of the existing paper, a single commutation overlap angle μ is calculated via (18) to represent the commutation process of all diodes [9]

$$\mu=\cos^{-1}\left(1-2\omega L_r\cdot i_{dc}\Big/\left(\sqrt{3}V_s\right)\right) \tag{18}$$

where V_s is the root mean square of the ac side voltage.

However, this is inaccurate due to fluctuations in the current on the dc side and the fact that the ac side voltage may not adhere to a standard sinusoidal waveform [14], even with ac filters configured at the PCC. Since μ_i is not a state variable, it is implicitly embedded in the differential equation and cannot be explicitly calculated, complicating the solution of (17). As shown in Fig. 4(c) and (d), the currents i_{j1}, i_{j2} cross zero sequentially in a specific order during the second type of switching, allowing its scalar function to be rewritten as

$$h_{2i}\left(x,t\right)=i=\begin{cases}i_{c1},i=1,7\\ i_{c2},i=2,8\\ i_{b1},i=3,9\\ i_{b2},i=4,10\\ i_{a1},i=5,11\\ i_{a2},i=6,12\end{cases}. \tag{19}$$

Therefore, the corresponding saltation matrix can be expressed as

$$\boldsymbol{S}_{2i}=\boldsymbol{I}+\frac{\left(\boldsymbol{f}_{2i}\left(\boldsymbol{x}\left(t_{2i-1}\right),t_{2i-1}\right)-\boldsymbol{f}_{2i-1}\left(\boldsymbol{x}\left(t_{2i-1}\right),t_{2i-1}\right)\right)\cdot\left(\frac{\partial i}{\partial \boldsymbol{x}}\right)^{T}}{\left(\frac{\partial i}{\partial \boldsymbol{x}}\right)^{T}\cdot\boldsymbol{f}_{2i-1}\left(\boldsymbol{x}\left(t_{2i-1}\right),t_{2i-1}\right)}. \tag{20}$$

As shown by the asterisk in Fig. 4(c), the currents i_{j1}, i_{j2} also cross zero sequentially during the first type of switching. When this is chosen as a scalar function, the absence of a time-dependent term in $h(\boldsymbol{x}, t)$ and the condition $\boldsymbol{n}^{\mathrm{T}}\boldsymbol{f}_{2i\text{-}2}=0$ imply that the trajectory is tangent to $h(\boldsymbol{x}, t)$ at the time $t_{2i\text{-}2}$, resulting in $\boldsymbol{S}_{2i\text{-}1}$ being infinite. Therefore, it is crucial to note that if the solution $\boldsymbol{x}(t)$ slides along the selected switching boundary during switching, it will invalidate the Filippov theory [25], necessitating careful selection of $h(\boldsymbol{x}, t)$.

Equations (16) and (20) provide the general expression for the saltation matrix of the studied system, with detailed derivation results available in Appendix B. Combining the results from Section III-A and III-B, the small-signal model of the system over the entire period is shown in Fig. 5. It can be observed that in each interval, the small-signal model is described by (11), while the saltation matrix at the switching instant connects the two intervals before and after the switching instant.

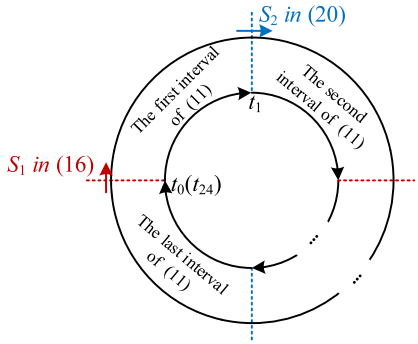

Fig. 5. Small-signal model of the studied system over the entire period.

C. Time Domain Validation

The piecewise small-signal model of the studied system is verified by comparing its dynamic responses to those of an electromagnetic transient model in MATLAB/ Simulink. The parameters of the studied system are detailed in Table I, while the design of control parameters refers to [11], [28].

Additionally, to illustrate the impact of switching dynamics of DR and the assumptions involved in calculating the commutation overlap angle on the analysis results, a harmonic state space model (HSSM) is constructed based on [9]. In HSSM, the switching dynamics of DR are represented by switching functions, and (18) is used to calculate the required commutation overlap angle. According to [34], capturing the dynamics of CCSC requires six-order truncation; therefore, frequency coupling up to six-order is considered.

A small disturbance of 0.02 p.u. is applied to u_{d+}^{*} (i.e., the reference for the d-axis component of PSTVC of MMC) at 2 s. The time-domain simulation results are shown in Fig. 6. From Fig. 6(a) and (b), it is evident that while HSSM captures the low-frequency dynamics of i_{dc}, it fails to reflect the 12 pulsations of i_{dc} per cycle due to switching, whereas the piecewise model accurately represents this behavior. As illustrated in Fig. 6(c) and (d), the positive sequence d-axis component of PCC voltage, $u_{\mathrm{pcc\_}d+}$, exhibits 12/24 pulsations in one cycle, indicating the presence of at least the 11/13th and 23/25th harmonics at the ac side, even with the ac filter configured. Due to the pulsations in the dc side current and the non-standard sinusoidal voltage on the ac side, the commutation overlap angle μ calculated by (18) does not accurately reflect the switching behaviors. This highlights that a single commutation overlap angle cannot fully represent the commutation processes of all diodes, particularly when there are significant pulsations on both the ac and dc sides.

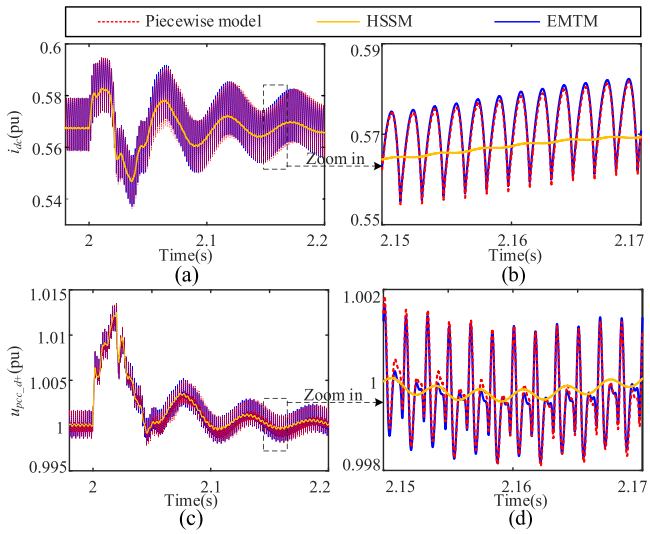

Fig. 6. (a) Dynamic responses of the three models when a disturbance of 0.02 p.u. is applied to u^*_{d+}. $i_{\rm dc}$. (b) Its zoomed-in waveform. (c) Positive sequence d-axis component of $u_{\rm pcc}$ and (d) its zoomed-in waveform.

IV. Small-Signal Stability Analysis

A. Stability Analysis Method

1) Floquet Theory: The small-signal model of a system that is smooth over the entire period is shown in (10), which is linear and time-periodic. Its fundamental-solution matrix can be expressed as $\boldsymbol{\Phi}(t, t_0)$ and satisfies

$$\Delta \boldsymbol{x}\left(t\right) = \boldsymbol{\Phi}\left(t, t_0\right) \Delta \boldsymbol{x}\left(t_0\right) \tag{21}$$

where $\boldsymbol{\Phi}(t, t_0)$, also known as the state transition matrix (STM), represents the transfer of states $\Delta \boldsymbol{x}$ from time t_0 to t.

By setting the start time $t_0 = 0$, and replacing t with T, $\boldsymbol{\Phi}(T, 0)$ reflects the state transfer over a complete period. The eigenvalues of $\boldsymbol{\Phi}(T, 0)$ are called Floquet multipliers. According to Floquet theory, the system is asymptotically stable if all Floquet multipliers lie within the unit circle in the complex plane, whereas it is unstable if any Floquet multipliers lie outside the unit circle. To further characterize the oscillation frequency, $\boldsymbol{\Phi}(T, 0)$ can be transformed as follows:

$$\boldsymbol{Q} = ln\left(\boldsymbol{\Phi}\left(T, 0\right)\right)/T. \tag{22}$$

The eigenvalues of $\boldsymbol{Q}$ are known as Floquet exponents. The frequency derived from the imaginary part of these eigenvalues is referred to as the modal frequency. It may differ from the actual oscillation frequency by nf_0, where n is an integer and f_0 is the fundamental frequency of the power grid.

2) Applying Floquet Theory to the Studied System: To apply Floquet theory to the studied piecewise smooth system, the relevant STM after one cycle need to be calculated. Based on the piecewise small-signal model developed in Section III, the STM after one cycle is thus composed of piecewise STMs before and after each switching, along with the saltation matrix during switching.

The small-signal model for each interval has been derived in Section III-A, as shown in (11). Therefore, the STM for each interval can be expressed as $\boldsymbol{\Phi}(t_i, t_{i\text{-}1})$, abbreviated as $\boldsymbol{\Phi}_i$, which reflects the state transfer of the system within each interval

$$\begin{bmatrix}\Delta \boldsymbol{x}_p\left(t_i\right) \\ \Delta \boldsymbol{x}_o\left(t_i\right)\end{bmatrix} = \boldsymbol{\Phi}\left(t_i, t_{i-1}\right) \begin{bmatrix}\Delta \boldsymbol{x}_p\left(t_{i-1}\right) \\ \Delta \boldsymbol{x}_o\left(t_{i-1}\right)\end{bmatrix}. \tag{23}$$

Although $\boldsymbol{\Phi}_i$ can be obtained through numerical integration [11], to enhance computational efficiency, this article employs the 'exponentials' method for approximating the computation of $\boldsymbol{\Phi}_i$ [32], [33]. This method divides the time interval $[t_{i\text{-}1}, t_i]$ into N subintervals, with the step size $\Delta t = (t_i\text{-}t_{i\text{-}1})/N$. If the step size Δt is sufficiently small, then $\boldsymbol{J}_i(t)$ within each subinterval can be considered constant, $\boldsymbol{J}_i(t) = [\boldsymbol{J}_{pi}(t)\, \boldsymbol{J}_o(t)]^T$. Consequently, $\boldsymbol{\Phi}_i$ can be computed as follows:

$$\boldsymbol{\Phi}_i \approx \prod_{k=1}^{N} e^{\boldsymbol{J}_i\left(t_k\right)\Delta t}. \tag{24}$$

Combining with the saltation matrices at switching instants, the STM after one cycle can be expressed as

$$\boldsymbol{\Phi}\left(T, 0\right) = \boldsymbol{\Phi}_{24}\boldsymbol{S}_{24}\cdots\boldsymbol{S}_2\boldsymbol{\Phi}_1\boldsymbol{S}_1. \tag{25}$$

It should be noted that due to the presence of redundant state variables, the eigenvalues of (25), i.e., Floquet multipliers, include (1, 0) in the complex plane, which implies the Floquet exponents located at the origin, but this does not affect the stability analysis.

B. Case Study

In this part, eigenvalue analysis method is employed to evaluate the impact of different controllers on small-signal stability. The advantage of the piecewise model is demonstrated by comparing its eigenvalue analysis results with those from HSSM. The stability analysis results are validated through electromagnetic transient simulations. The studied system's parameters are listed in Table I.

1) Case I. Influence of PSTVC on Small-Signal Stability: To investigate the impact of PSTVC, its bandwidth (BW) is adjusted within the range of 2 to 5 Hz. The eigenvalue locus for the piecewise model and HSSM is shown in Fig. 7(a) and (b), respectively. As BW decreases, a pair of eigenvalues of both models crosses the imaginary axis into the left half-plane, indicating potential instability. However, significant differences emerge between the analysis results of the piecewise model and HSSM. As shown in Fig. 7(c), for BW = 2.39 Hz, the eigenvalues with maximum real parts (MRPs) of the piecewise model are $0.50 \pm 9.53 \times 2\pi j$ (where j denotes the imaginary unit), indicating instability, while the eigenvalues with MRPs of HSSM are $-0.76 \pm 9.47 \times 2\pi j$, suggesting stability.

To verify the above eigenvalue analysis results, an electromagnetic transient simulation is conducted. The PSTVC BW changes from 5 to 2.39 Hz at 2s. The waveform of $u_{\rm pcc\_d+}$, shown in Fig. 8(a) and (b), exhibits a divergent oscillation and contains characteristic harmonics. According to the FFT analysis results displayed in Fig. 8(c), $u_{\rm pcc\_d+}$ contains at least 12th, 24th, and 36th harmonics. Additionally, the oscillation frequency of the unstable mode is identified as 9.5 Hz, which closely aligns with the analysis results of the piecewise model.

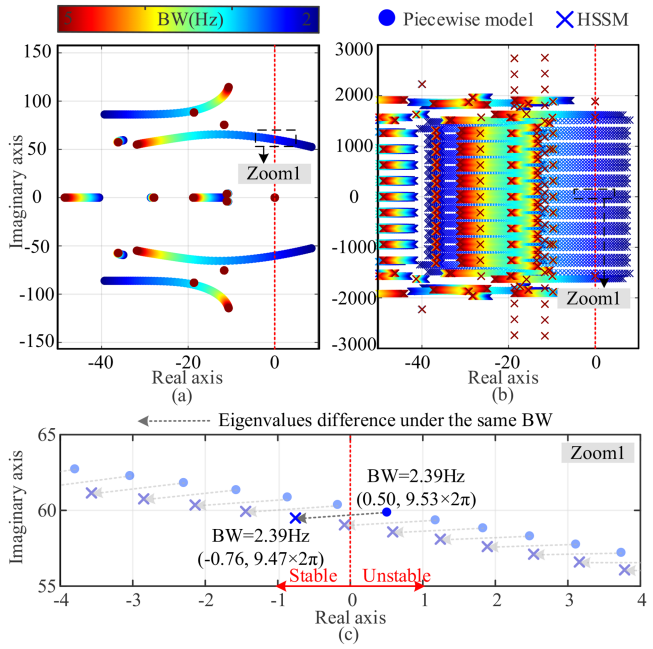

Fig. 7. Eigenvalue locus of the (a) piecewise model and (b) HSSM with the change of PSTVC BW. (c) Comparison of eigenvalues between the piecewise model and HSSM in Zoom1.

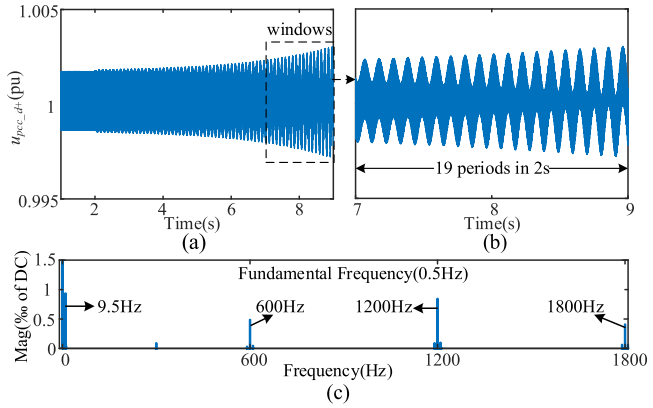

Fig. 8. (a) Electromagnetic transient simulation results of $u_{\mathrm{pcc\_}d+}$. (b) Zoomed oscillation waveform. (c) FFT analysis results of $u_{\mathrm{pcc\_}d+}$.

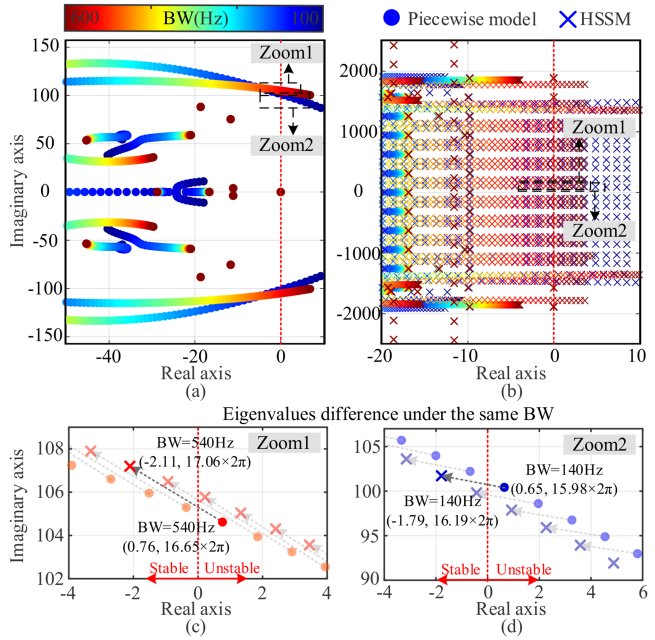

Fig. 9. (a) Eigenvalue locus of the piecewise model and (b) HSSM with the change of PSDMC BW. Comparison of eigenvalues between the piecewise model and HSSM in (c) Zoom 1 and (d) Zoom 2.

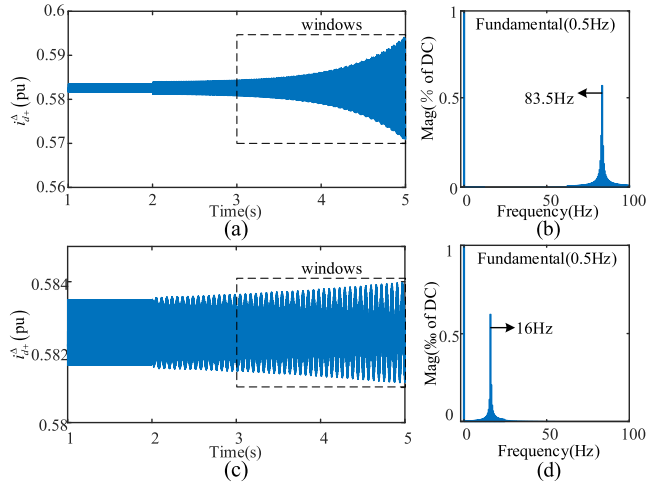

Fig. 10. (a) Electromagnetic transient simulation results of i^{Δ}_{d+} when PSDMC BW changes to 540Hz and (b) its FFT analysis results, (c) i^{Δ}_{d+} when PSDMC BW changes to 140Hz and (d) its FFT analysis results.

Overall, the simulation results confirm that the piecewise model accurately reflects the small-signal stability of the system, while the HSSM yields inaccurate results.

2) Case II. Influence of PSDMC on Small-Signal Stability: As a critical component of MMC control systems, the parameters of PSDMC also significantly influence system stability. Similar to the analysis of PSTVC, this part examines the effect of PSDMC BW on system stability.

Fig. 9(a) and (b) show the eigenvalue locus for both models with the change of PSDMC BW. The piecewise model indicates that when BW is greater than 540 Hz or less than 140 Hz, the eigenvalue locus crosses the imaginary axis into the right half-plane, leading to system instability. As shown in Fig. 9(c) and (d), the unstable range arises from two different modes, with eigenvalues of $0.76\pm16.65\times2\pi j$ and $0.65\pm15.98\times2\pi j$ under these boundary parameters. In contrast, HSSM suggests that the system remains stable under the same boundary parameters, with eigenvalues of -2.11±16.65×2πj and -1.79±16.19×2πj, respectively.

The time-domain simulation is conducted to verify the above analysis. At 2s, PSDMC BW is changed from 183Hz to 540 Hz and 140 Hz, respectively. The waveforms of the positive d-axis component of DMC currents i^{Δ}_{d+} are shown in Fig. 10(a) and (c). It can be observed that under these boundary parameters, i^{Δ}_{d+} appears gradual oscillations. The FFT analysis results,

Fig. 11. Hardware-in-the-loop experimental platform.

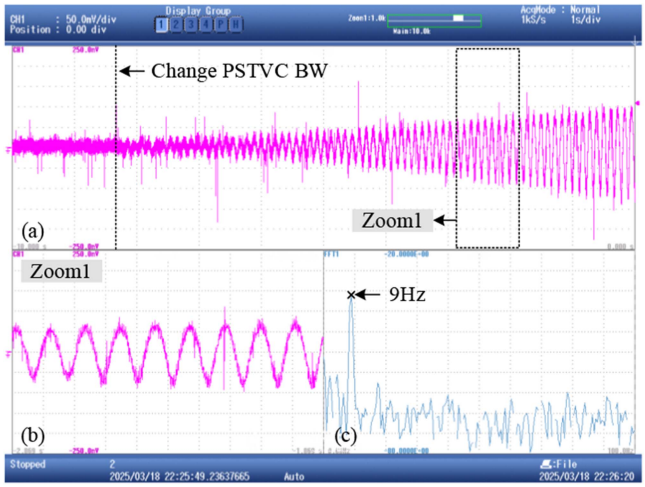

Fig. 12. Experimental results of case I: PSTVC BW is changed from 5 to 2.39 Hz. (a) u_{pcc_d+}. (b) Zoomed oscillation waveform. (c) FFT for the oscillation component.

displayed in Fig. 10(b), reveal that at BW = 540 Hz, the actual oscillation frequency is 83.5 Hz, which is shifted by $2f_0$ compared to the modal frequency. Meanwhile, Fig. 10(d) shows that at BW = 140Hz, the actual oscillation frequency is 16Hz, which is the same as the modal frequency. The time-domain simulation results validate the accuracy of the analysis results.

C. Discussion of Stability Analysis Results

This part further discusses the stability analysis results. The discrepancy in stability analysis arises from the differential treatment of the switching dynamics of DR: the piecewise model

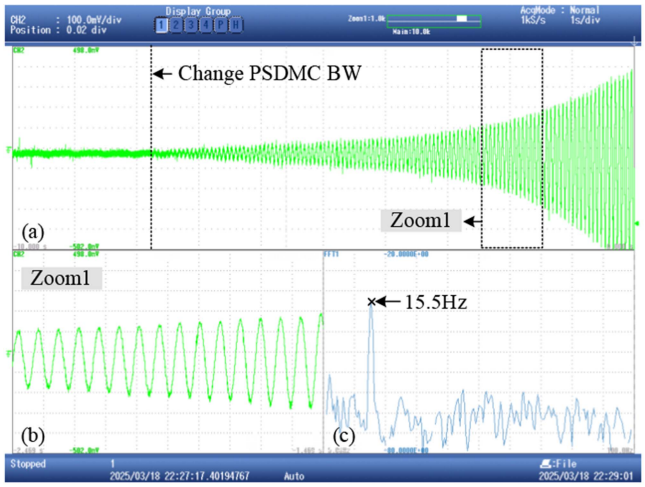

Fig. 13. Experimental results of case II: PSDMC BW is changed from 183 to 140 Hz. (a) i_{d+}^{Δ}. (b) zoomed oscillation waveform. (c) FFT for the oscillation component.

utilizes saltation matrices while HSSM employs switching functions. Under original parameters, we calculated the saltation matrices at switching instants of the piecewise model. Excluding the identity matrices, the elements of the saltation matrix for the first type of switching event (occurring at phase-to-phase voltage zero-crossings) are around $1e^{-5}$, indicating a small impact on stability. In contrast, for the second type of switching event, the elements reach up to $1e^{1}$, comparable to the order of magnitude of the elements of the STM after one cycle. It indicates that the end of commutation processes significantly impacts the system stability. However, in HSSM, the commutation process is represented by the commutation overlap angle (18) embedded in the switching function. The assumptions in calculating commutation overlap angle diminish the accuracy of HSSM.

Additionally, diode switching induces non-differentiable points in both the ac and dc side of DR, generating theoretically infinite characteristic harmonics (ac: 12k±1, dc: 12k, where $k = 1, 2, \ldots$). The piecewise model fully captures these harmonics via saltation matrices. However, for practical analysis, the HSS modeling method needs to impose truncation. Given modeling feasibility and computational burden, the truncation order of HSSM is typically not excessively high. Insufficient truncation order results in the loss of critical switching dynamics.

Consequently, HSSM yields inaccurate analysis results. This further emphasizes the critical importance of precise modeling of switching dynamics.

V. Experimental Results

To validate the simulation results of the case study, hardware-in-the-loop testing was performed using RT-LAB (OP5700, equipped with 2 Intel i7 6-Core CPUs at 3.3 GHz). As depicted in Fig. 11, the experimental platform consists of a host computer, oscilloscope, digital signal processor (DSP), OP5700 real-time simulator, and a power supply unit, all interconnected via signal interfaces. The simulator executes the system's circuit model,

while the DSP implements the control algorithm. All parameters are consistent with those provided in Table I.

Fig. 12 presents the experimental results for case I. When PSTVC BW is changed from 5 to 2.39 Hz, the waveform of $u_{\mathrm{pcc\_}d+}$ shows divergent oscillations and the system becomes unstable. The FFT analysis in Fig. 12(c) identifies the oscillation frequency as 9 Hz. These experimental results align with the time-domain simulations and stability analysis results derived from the piecewise model.

The stability analysis of case II was similarly validated through experimental testing. As shown in Fig. 13, reducing the PSDMC BW to 140 Hz induces unstable oscillations. The FFT analysis results in Fig. 13(c) reveal oscillation frequencies of 15.5 Hz, which closely match the simulation results.

VI. Conclusion

Following Filippov's theory, this article constructs the piecewise small-signal model of DR-MMC HVDC for OWFs, demonstrating significant potential application value. Unlike existing methods based on state-space averaging or switching functions, the proposed model fully captures the switching dynamics and commutation process of DR. Combined with Floquet theory, we further analyze the influence of parameters on system stability. The analysis results from the proposed model align more closely with electromagnetic transient tests conducted in RT-LAB compared to HSSM. As system parameters change and stability gradually weakens, HSSM tends to yield inaccurate stability boundaries. Therefore, we emphasize that the switching dynamics and commutation process of DR cannot be overlooked or simplified based on assumptions in this scenario, as they significantly affect the stability analysis results. Furthermore, the small-signal modeling and stability analysis method introduced in this article has strong applicability and will be applied in more scenarios of power electronics-dominated power systems in the future.

Appendix

A. Detailed Mathematical Model for Each Interval

Given the large number of expressions for the 24 intervals, we select one interval from each of the 12 commutation processes and 12 noncommutation processes and derive its expression. The remaining intervals can be derived similarly. The first interval is defined as VT156/56 conduction (commutation process), and the second interval as VT16/56 conduction (noncommutation process). The corresponding differential equations $\dot{\boldsymbol{x}}_p = \boldsymbol{f}_{p1}$ and $\dot{\boldsymbol{x}}_p = \boldsymbol{f}_{p2}$ and are derived for each interval, respectively.

When VT156/56 is conducted, the dynamics of the dc side and the commutation process in this interval are governed by (6) and (7). Further solutions can be derived as follows:

$$\frac{di_{a1}}{dt} = \frac{\sum_{x=a,b,c} u_{mx}^{\Sigma} - (R_{\mathrm{arm}} + 3R_d)\sum_{x=a,b,c} i_x^{\Sigma} - 3C_u}{2L_{\mathrm{arm}} + 6L_d + 21L_r} + \frac{(L_{\mathrm{arm}} + 3L_d + 9L_r)(u_{a1} - u_{c1})}{L_r(2L_{\mathrm{arm}} + 6L_d + 21L_r)} \tag{A1}$$

$$\frac{di_j^{\Sigma}}{dt} = -\frac{\begin{pmatrix} L_{\mathrm{arm}}(u_{a1} - u_{c1}) + (2L_d + 7L_r)\sum_{x=a,b,c} u_{mx}^{\Sigma} + 2L_{\mathrm{arm}}C_u \\ +(2L_{\mathrm{arm}}R_d - 2L_dR_{\mathrm{arm}} - 7L_rR_{\mathrm{arm}})\sum_{x=a,b,c} i_x^{\Sigma} \end{pmatrix}}{L_{\mathrm{arm}}(2L_{\mathrm{arm}} + 6L_d + 21L_r)} + \frac{1}{L_{\mathrm{arm}}}\left(u_{mj}^{\Sigma} - R_{\mathrm{arm}}i_j^{\Sigma}\right) \tag{A2}$$

$$C_u = -u_{a1} + u_{b2} - u_{c2} + u_{b1} + \frac{u_{dc}}{2}. \tag{A3}$$

According to the DR topology shown by the red solid line in Fig. 1(c), in this interval, the remaining states i_{b1}, i_{c1}, and $\boldsymbol{i}_{j2}$ in $\boldsymbol{x}_p$ are not independent and can be derived from i_{a1} and $\boldsymbol{i}_j^{\Sigma}$ as follows:

$$i_{b1} = -\sum_{x=a,b,c} i_x^{\Sigma} \;\vdots\; i_{c1} = \sum_{x=a,b,c} i_x^{\Sigma} - i_{a1} \tag{A4}$$

$$i_{a2} = 0 \;\vdots\; i_{b2} = -\sum_{x=a,b,c} i_x^{\Sigma} \;\vdots\; i_{c2} = \sum_{x=a,b,c} i_x^{\Sigma}. \tag{A5}$$

Thus, $\dot{\boldsymbol{x}}_p = \boldsymbol{f}_{p1}$ can be specified by (A1), (A2), (A4), and (A5).

When VT16/56 is conducted, only the dc side dynamics need to be derived in this interval. Based on the DR topology shown by the blue dashed line in Fig. 1(c), it can be derived as follows:

$$\begin{pmatrix} -u_{a1} + u_{b2} - u_{c2} + u_{b1} \\ +(L_d + 4L_r)\cdot\sum_{x=a,b,c}\frac{di_x^{\Sigma}}{dt} + R_d\sum_{x=a,b,c} i_x^{\Sigma} \end{pmatrix} + \frac{u_{dc}}{2} + \left(L_{\mathrm{arm}}\frac{di_j^{\Sigma}}{dt} + R_{\mathrm{arm}}i_j^{\Sigma} - u_{mj}^{\Sigma}\right) = 0. \tag{A6}$$

Substituting (A3) into (A6) and solving further yields the following:

$$\frac{di_j^{\Sigma}}{dt} = -\frac{\begin{pmatrix} (L_d + 4L_r)\sum_{x=a,b,c} u_{mx}^{\Sigma} + L_{\mathrm{arm}}C_u + \\ (L_{\mathrm{arm}}R_d - L_dR_{\mathrm{arm}} - 4L_rR_{\mathrm{arm}})\sum_{x=a,b,c} i_x^{\Sigma} \end{pmatrix}}{L_{\mathrm{arm}}(L_{\mathrm{arm}} + 3L_d + 12L_r)} + \frac{1}{L_{\mathrm{arm}}}\left(u_{mj}^{\Sigma} - R_{\mathrm{arm}}i_j^{\Sigma}\right). \tag{A7}$$

In this interval, the remaining states $\boldsymbol{i}_{j1}$ and $\boldsymbol{i}_{j2}$ in $\boldsymbol{x}_p$ are all not independent and can be expressed in terms of i_j^{Σ} as follows:

$$i_{a1} = \sum_{x=a,b,c} i_x^{\Sigma} \;\vdots\; i_{b1} = -\sum_{x=a,b,c} i_x^{\Sigma} \;\vdots\; i_{c1} = 0 \tag{A8}$$

$$i_{a2} = 0 \;\vdots\; i_{b2} = -\sum_{x=a,b,c} i_x^{\Sigma} \;\vdots\; i_{c2} = \sum_{x=a,b,c} i_x^{\Sigma}. \tag{A9}$$

Therefore, $\dot{\boldsymbol{x}}_p = \boldsymbol{f}_{p2}$ can be specified by (A7), (A8), and (A9).

B. Detailed Saltation Matrix of the Studied System

In this part, the saltation matrices $\boldsymbol{S}_1$ and $\boldsymbol{S}_2$, corresponding to the two types of switching events, are presented as examples, and their detailed derivations are provided. The other saltation matrices can be derived similarly.

The saltation matrix corresponding to the first type of switching event is given in (16). By substituting $i = 1$, we obtain

$$\boldsymbol{S}_1 = \boldsymbol{I} + \frac{\left(\boldsymbol{f}_1\left(\boldsymbol{x}\left(t_0\right), t_0\right) - \boldsymbol{f}_{24}\left(\boldsymbol{x}\left(t_0\right), t_0\right)\right) \cdot \left(\frac{\partial u_{pp}}{\partial \boldsymbol{x}}\right)^T}{\left(\frac{\partial u_{pp}}{\partial \boldsymbol{x}}\right)^T \cdot \boldsymbol{f}_{24}\left(\boldsymbol{x}\left(t_0\right), t_0\right)} \tag{B1}$$

where $\boldsymbol{f}_1 = [\boldsymbol{f}_{p1}\ \boldsymbol{f}_{\mathrm{o}}]^T$, $\boldsymbol{f}_{24} = [\boldsymbol{f}_{p24}\ \boldsymbol{f}_{\mathrm{o}}]^T$. The u_{pp} at this time can be obtained from (15)

$$u_{pp} = u_{a1} - u_{c1} = T_{\mathrm{DR}}\left(u_{\mathrm{pcca}} - u_{\mathrm{pccc}}\right) \tag{B2}$$

where T_{DR} is the transformer ratio of DR, $u_{\mathrm{pcc}a}$ and $u_{\mathrm{pcc}c}$ is PCC voltage.

Since $\boldsymbol{x} = [\boldsymbol{x}_p\ \boldsymbol{x}_o]^T$, assuming $\boldsymbol{u}_{\mathrm{pcc}}$ is the first three state variables in $\boldsymbol{x}_o$, $\partial u_{pp}/\partial \boldsymbol{x}$ can be derived as follows:

$$\frac{\partial u_{pp}}{\partial \boldsymbol{x}} = T_{\mathrm{DR}}\left[\boldsymbol{0}_{1\times n_p}\ 1\ 0\ -1\ \boldsymbol{0}_{1\times(n_o-3)}\right] T \tag{B3}$$

where $n_p = 9$ is the dimension of $\boldsymbol{x}_p$, and n_o is the dimension of $\boldsymbol{x}_o$.

By substituting (B3) into (B1), the following result can be obtained as

$$\boldsymbol{S}_1 = \boldsymbol{I} + \frac{\begin{bmatrix}\left(\boldsymbol{f}_{p1} - \boldsymbol{f}_{p24}\right)\big|_{\boldsymbol{x}(t_0),t_0} \\ \boldsymbol{0}_{n_o\times 1}\end{bmatrix} \cdot \left[\boldsymbol{0}_{1\times n_p} \,\vdots\, 1\ 0\ -1\ \boldsymbol{0}_{1\times(n_o-3)}\right]}{\left[\boldsymbol{0}_{1\times n_p} \,\vdots\, 1\ 0\ -1\ \boldsymbol{0}_{1\times(n_o-3)}\right] \cdot \begin{bmatrix}\boldsymbol{f}_{p24}\big|_{\boldsymbol{x}(t_0),t_0} \\ \boldsymbol{f}_o\big|_{\boldsymbol{x}(t_0),t_0}\end{bmatrix}} \tag{B4}$$

where $\boldsymbol{f}_{p1}$ is provided in Appendix A. The derivation of $\boldsymbol{f}_{p24}$ follows the same process as that of $\boldsymbol{f}_{p2}$. Equation (B4) can be further simplified as

$$\boldsymbol{S}_1 = \boldsymbol{I} + \frac{\begin{bmatrix}\left(\boldsymbol{f}_{p1} - \boldsymbol{f}_{p24}\right)\big|_{\boldsymbol{x}(t_0),t_0} \\ \boldsymbol{0}_{n_o\times 1}\end{bmatrix} \cdot \left[\boldsymbol{0}_{1\times n_p} \,\vdots\, 1\ 0\ -1\ \boldsymbol{0}_{1\times(n_o-3)}\right]}{\frac{d(u_{\mathrm{pcca}}-u_{\mathrm{pccc}})}{dt}\big|_{t_0}}. \tag{B5}$$

The saltation matrix corresponding to the second type of switching event is shown in (20). By substituting $i = 1$, we obtain

$$\boldsymbol{S}_2 = \boldsymbol{I} + \frac{\left(\boldsymbol{f}_2\left(\boldsymbol{x}\left(t_1\right), t_1\right) - \boldsymbol{f}_1\left(\boldsymbol{x}\left(t_1\right), t_1\right)\right) \cdot \left(\frac{\partial i}{\partial \boldsymbol{x}}\right)^T}{\left(\frac{\partial i}{\partial \boldsymbol{x}}\right)^T \cdot \boldsymbol{f}_1\left(\boldsymbol{x}\left(t_1\right), t_1\right)}. \tag{B6}$$

Equation (19) shows that $i = i_{c1}$ at this time. Therefore, $\partial i/\partial \boldsymbol{x}$ can be derived as follows:

$$\frac{\partial i}{\partial \boldsymbol{x}} = \left[0\ \ 0\ \ 1 \,\vdots\, \boldsymbol{0}_{1\times(n_p-3)} \,\vdots\, \boldsymbol{0}_{1\times n_o}\right] T. \tag{B7}$$

Substituting (B7) into (B6) and simplifying further yields

$$\boldsymbol{S}_2 = \boldsymbol{I} + \frac{\begin{bmatrix}\left(\boldsymbol{f}_{p2} - \boldsymbol{f}_{p1}\right)\big|_{\boldsymbol{x}(t_1),t_1} \\ \boldsymbol{0}_{n_o\times 1}\end{bmatrix} \cdot \left[0\ \ 0\ \ 1\ \ \boldsymbol{0}_{1\times(n_p-3)}\ \ \boldsymbol{0}_{1\times n_o}\right]}{\frac{di_{c1}}{dt}\big|_{t_1}}. \tag{B8}$$

It can be observed that only a small number of elements in $\boldsymbol{S}_1$ and $\boldsymbol{S}_2$ are non-zero. Therefore, the saltation matrix is sparse.

C. Parameters of the Studied System

TABLE I
PARAMETERS OF THE STUDIED SYSTEM

Symbol	Values	Symbol	Values	Segment
S_{base}	500 MW	ω_c	$1.414\omega_0$	MMC
f_{base}	50 Hz	a_f	$2\omega_0$	
U_{base}	160 kV	PSTVC (T_{vp}, BW)	2, 5	
U_{dcbase}	320 kV	NSTVC (T_{vn}, BW)	2, 5	
$L_{\mathrm{t\_mmc}}$	27.7 mH	PSDMC (ζ_{ip}, BW)	1.6, 183	
T_{MMC}	66 kV/160 kV	NSDMC (ζ_{in}, BW)	1.6, 183	
L_{arm}	40 mH	*CCSC* (ζ_{cir}, BW)	1, 180	
C_{arm}	20.57 μF			
S_{base}	250 MW	L_r	0.18 p.u.	DR
T_{DR}	66 kV/67 kV			
S_{base}	1000 MW	ω_c	$1.414\omega_0$	WT
S_{base} of each WT	2 MW	a_f	$2\omega_0$	
U_{base}	690 V	PSCC (ζ_{ip}, BW)	1.6, 300	
U_{dcbase}	1200 V	NSCC (ζ_{in}, BW)	1.6, 300	
$L_{\mathrm{t\_vsc}}, R_{\mathrm{t\_vsc}}$	0.15 p.u., 0.003 p.u.	DVC (ζ_{dv}, BW)	0.6, 20	
T_{VSC}	690 V/66 kV	PLL (ζ_{pll}, BW)	0.7, 25	
$C_{\mathrm{dc\_vsc}}$	0.09 F	I_{in}	0.6 p.u.	
L_{ac}, R_{ac}, C_{ac}	60 mH, 0 Ω, 26 μF	$L_{\mathrm{dc}}, R_{\mathrm{dc}}$	48 mH, 0 Ω	Transmission line
$u_{\mathrm{dc}}/2$	335 kV			

The parameters of DR's AC filters refer to [9].

REFERENCES

[1] J. Deng et al., "A review of system topologies, key operation, and control technologies for offshore wind power transmission based on HVDC," *IET Gener. Transmiss. Distrib.*, vol. 17, no. 15, pp. 3345–3363, Jun. 2023.

[2] F. Li, L. Lin, Y. Li, X. Shi, J. Hu, and J. Zhu, "Synchronization stability of the MMC-connected wind farm under severe asymmetrical faults," *IEEE J. Emerg. Sel. Top. Circuits Syst.*, vol. 13, no. 3, pp. 680–691, Sep. 2023.

[3] M. A. Perez, S. Bernet, J. Rodriguez, S. Kouro, and R. Lizana, "Circuit topologies, modeling, control schemes, and applications of modular multilevel converters," *IEEE Trans. Power Electron.*, vol. 30, no. 1, pp. 4–17, Jan. 2015.

[4] J. Sun et al., "Renewable energy transmission by HVDC across the continent: System challenges and opportunities," *CSEE J. Power Energy Syst.*, vol. 3, no. 4, pp. 353–364, Dec. 2017.

[5] R. Blasco-Gimenez, S. Añó-Villalba, J. Rodríguez-D'Derlée, F. Morant, and S. Bernal-Perez, "Distributed voltage and frequency control of offshore wind farms connected with a diode-based HVDC link," *IEEE Trans. Power Electron.*, vol. 25, no. 12, pp. 3095–3105, Dec. 2010.

[6] Y. Chang and X. Cai, "Hybrid topology of a diode-rectifier-based HVDC system for offshore wind farms," *IEEE J. Emerg. Sel. Top. Power Electron.*, vol. 7, no. 3, pp. 2116–2128, Sep. 2019.
[7] R. Li and L. Xu, "A unidirectional hybrid HVDC transmission system based on diode rectifier and full-bridge MMC," *IEEE J. Emerg. Sel. Top. Power Electron.*, vol. 9, no. 6, pp. 6974–6984, Dec. 2021.
[8] G. Zhang, W. Xiang, X. Chen, and J. Wen, "Capacity design of cascaded diode rectifier-MMC based HVDC for offshore wind farm integration," *IEEE Trans. Power Del.*, vol. 39, no. 5, pp. 2908–2919, Oct. 2024.
[9] G. Zhang, W. Xiang, and J. Wen, "Impedance modeling and stability analysis of DR-MMC based hybrid HVDC for offshore wind farm integration," *IEEE Trans. Power Del.*, vol. 38, no. 6, pp. 4397–4409, Dec. 2023.
[10] J. Freytes et al., "Improving small-signal stability of an MMC with CCSC by control of the internally stored energy," *IEEE Trans. Power Del.*, vol. 33, no. 1, pp. 429–439, Feb. 2018.
[11] J. Zhu, J. Hu, S. Wang, and M. Wan, "Small-signal modeling and analysis of MMC under unbalanced grid conditions based on linear time-periodic (LTP) method," *IEEE Trans. Power Del.*, vol. 36, no. 1, pp. 205–214, Feb. 2021.
[12] J. Zhu, J. Hu, Y. Li, S. Ma, and T. Wang, "Small-signal stability of MMC grid-tied system under two typical unbalanced grid conditions," *IEEE Trans. Ind. Appl.*, vol. 58, no. 4, pp. 5005–5014, Jul./Aug. 2022.
[13] J. Zhu, Z. Guo, J. Hu, S. Ma, and J. Guo, "Truncation number selection of harmonic state-space model based on the Floquet characteristic exponent," *IEEE Trans. Ind. Electron.*, vol. 70, no. 3, pp. 3222–3228, Mar. 2023.
[14] L. Chen, J. Wang, Z. Li, C. Guo, B. Zhang, and Z. Li, "Steady-state analysis of the DR-MMC based hybrid topology for offshore wind power transmission," *IEEE Trans. Power Electron.*, vol. 40, no. 2, pp. 3177–3188, Feb. 2025.
[15] V. Caliskan, D. J. Perreault, T. M. Jahns, and J. G. Kassakian, "Analysis of three-phase rectifiers with constant-voltage loads," in *Proc. 30th Annu. IEEE Power Electron. Specialists Conf.*, 1999, pp. 715–720.
[16] L. Hu and R. Yacamini, "Harmonic transfer through converters and HVDC links," *IEEE Trans. Power Electron.*, vol. 7, no. 3, pp. 514–525, Jul. 1992.
[17] R. D. Middlebrook and S. Cuk, "A general unified approach to modeling switching-converter power stages," in *Proc. IEEE Power Electron. Specialists Conf.*, 1976, pp. 18–34.
[18] D. Giaouris, S. Banerjee, B. Zahawi, and V. Pickert, "Stability analysis of the continuous-conduction-mode buck converter via Filippov's method," *IEEE Trans. Circuits Syst. I: Reg. Papers*, vol. 55, no. 4, pp. 1084–1096, May 2008.
[19] I. Dobson, "Stability of ideal thyristor and diode switching circuits," *IEEE Trans. Circuits Syst. I, Fundam. Theory Appl.*, vol. 42, no. 9, pp. 517–529, Sep. 1995.
[20] Z. Bing, K. J. Karimi, and J. Sun, "Input impedance modeling and analysis of line-commutated rectifiers," *IEEE Trans. Power Electron.*, vol. 24, no. 10, pp. 2338–2346, Oct. 2009.
[21] L. Yu, L. Xu, J. Zhu, and R. Li, "Impedance modelling and stability analysis of diode-rectifier based HVDC connected offshore wind farms," *IEEE Trans. Power Del.*, vol. 37, no. 1, pp. 591–602, Feb. 2022.
[22] B. Du, J. Zhu, J. Hu, Z. Guo, S. Ma, and J. Guo, "Small-signal modeling of LCC-HVDC considering switching dynamics based on the linear time-periodic (LTP) method," *IEEE Trans. Power Del.*, vol. 39, no. 5, pp. 2715–2728, Oct. 2024.
[23] E. Mollerstedt and B. Bernhardsson, "Out of control because of harmonics-an analysis of the harmonic response of an inverter locomotive," *IEEE Control Syst. Mag.*, vol. 20, no. 4, pp. 70–81, Aug. 2000.
[24] L. J. Bohmann and H. Feng, "Small signal transient stability of periodically switched circuits," in *Proc. 37th Midwest Symp. Circuits Syst.*, 1994, pp. 1299–1302.
[25] R. Leine and H. Nijmeijer, *Dynamics and Bifurcations of Non-Smooth Mechanical Systems*. Berlin, Germany: Springer, 2004.
[26] M. Amin and M. Molinas, "Understanding the origin of oscillatory phenomena observed between wind farms and HVDC systems," *IEEE J. Emerg. Sel. Top. Power Electron.*, vol. 5, no. 1, pp. 378–392, Mar. 2017.
[27] X. Wang and F. Blaabjerg, "Harmonic stability in power electronic-based power systems: Concept, modeling, and analysis," *IEEE Trans. Smart Grid*, vol. 10, no. 3, pp. 2858–2870, May 2019.
[28] L. Lin, Q. Zeng, J. Zhu, X. Shi, and J. Hu, "High-frequency oscillation mechanism analysis and suppression strategy of grid-forming control MMC-HVDC," *IEEE Trans. Power Del.*, vol. 38, no. 3, pp. 1588–1600, Jun. 2023.
[29] K. M. Alawasa, Y. A.-R. I. Mohamed, and W. Xu, "Modeling, analysis, and suppression of the impact of full-scale wind-power converters on subsynchronous damping," *IEEE Syst. J.*, vol. 7, no. 4, pp. 700–712, Dec. 2013.
[30] I. A. Hiskens and M. A. Pai, "Trajectory sensitivity analysis of hybrid systems," *IEEE Trans. Circuits Syst. I, Fundam. Theory Appl.*, vol. 47, no. 2, pp. 204–220, Feb. 2000.
[31] H. Wu, V. Pickert, D. Giaouris, and B. Ji, "Nonlinear analysis and control of interleaved boost converter using real-time cycle to cycle variable slope compensation," *IEEE Trans. Power Electron.*, vol. 32, no. 9, pp. 7256–7270, Sep. 2017.
[32] P. Friedmann, C. E. Hammond, and T. Woo, "Efficient numerical treatment of periodic systems with application to stability problems," *Int. J. Numer. Methods Eng.*, vol. 11, no. 7, pp. 1117–1136, Jan. 1977.
[33] L. Peletan, S. Baguet, M. Torkhani, and G. Jacquet-Richardet, "A comparison of stability computational methods for periodic solution of nonlinear problems with application to rotordynamics," *Nonlinear Dyn.*, vol. 72, no. 3, pp. 671–682, May 2013.
[34] J. Zhu, Y. Hou, J. Hu, Y. Li, and J. Guo, "Revealing 150 Hz oscillation of MMC-HVDC based on high-fidelity HSS model," *IEEE Trans. Ind. Electron.*, vol. 72, no. 2, pp. 2156–2159, Feb. 2025.

Zefei Wu received the B.Eng. degree in electrical engineering from Southwest Jiaotong University (SWJTU), Chengdu, China, in 2023. He is currently working toward the Ph.D. degree in electrical engineering with the State Key Laboratory of Advanced Electromagnetic Technology, School of Electrical and Electronic Engineering, HUST, Wuhan, China.

His research interests include small-signal modeling and stability analysis of power electronic-dominated power system.

Jianhang Zhu (Member, IEEE) received the B.Eng. degree in electrical engineering from the College of Water Resources and Architectural Engineering, Northwest A&F University, Xi'an, China, in 2014, and the Ph.D. degree in electrical engineering from the School of Electrical and Electronic Engineering, Huazhong University of Science and Technology (HUST), Wuhan, China, in 2020.

From 2020 to 2023, he was a Post-doctoral Fellow with HUST. In 2022, he was with the University of Hong Kong, Hong Kong, where he is currently a Research Scientist. His research interests include modeling and analysis of electromagnetic small-signal stability in power systems with renewable energy generations and high-voltage dc transmission.

Jiabing Hu (Senior Member, IEEE) received the B.Eng. and Ph.D. degrees in electrical engineering from the College of Electrical Engineering, Zhejiang University, Hangzhou, China, in 2004 and 2009, respectively.

From 2007 to 2008, he was funded by Chinese Scholarship Council as a Visiting Scholar with the Department of Electronic and Electrical Engineering, University of Strathclyde, Glasgow, U.K. From April 2010 to August 2011, he was a Post-Doctoral Research Associate with Sheffield Siemens Wind Power Research Center and the Department of Electronic and Electrical Engineering, University of Sheffield, Sheffield, U.K. Since September 2011, he has been a Professor with State Key Laboratory of Advanced Electromagnetic Technology, and School of Electrical and Electronic Engineering, Huazhong University of Science and Technology, Wuhan, China.

His current research interests include grid integration of large scale renewables and modeling, analysis, and control of power electronized power systems.

Zeren Guo (Student Member, IEEE) received the B.Eng. degree in electrical engineering in 2019 from Huazhong University of Science and Technology, Wuhan, China, where he is currently working toward the Ph.D. degree in electrical engineering with the State Key Laboratory of Advanced Electromagnetic Technology.

His research interests include small-signal modeling and stability analysis of power electronic-dominated power systems.

Buyang Du received the B.Eng. degree in electrical engineering in 2020 from Huazhong University of Science and Technology (HUST), Wuhan, China, where he is currently working toward the Ph.D. degree in electrical engineering with the State Key Laboratory of Advanced Electromagnetic Technology, School of Electrical and Electronic Engineering.

His current research interests include small-signal modeling, stability analysis, and control of power electronic-dominated power systems.

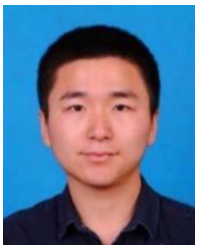

Yingbiao Li (Member, IEEE) received the B.S. degree from Wuhan University, Wuhan, China, in 2014, and the M.S. and Ph.D. degrees from China Electric Power Research Institute, Beijing, China, in 2017 and 2020, respectively, all in electrical engineering.

He is currently an Associate Research Fellow with the State Key Laboratory of Advanced Electromagnetic Technology (Huazhong University of Science and Technology) and Technology and the School of Electrical and Electronic Engineering, Huazhong University of Science and Technology, Wuhan, China. His main research interests include transient stability analysis of the power electronized power systems.

Jianbo Guo received the B.S. degree in electrical engineering from Huazhong University of Science and Technology, Wuhan, China, in 1982, and M.S. degree from China Electric Power Research Institute, Beijing, China, in 1984.

From 2010 to 2019, he was the Chairman of China Electric Power Research Institute. Since 2013, he has been an elected Academician of the Chinese Academy of Engineering, Beijing, China. He is currently the Deputy Chief Engineer with the State Grid Corporation of China, the Vice Chairman of China Electrical Engineering Society, and the Honorary Chairman of China Electric Power Research Institute. He has been dedicated to the clean use of energy and the development of environmentally friendly power grid. He has long engaged in power system analysis & control. He has made remarkable achievements in power grid planning, improving security, reliability and transfer capability of power grid, and security of wind power integration. As the Principal Investigator, he participated in Chinese National Programs for Three Gorges Power Transmission Project and many other important grid planning studies. He presided over the development plan for Chinese National Grid Interconnection Project (from 2020 to 2050). He successfully developed Thyristor Controlled Series Compensation and UHV series compensator (1000 kV) with proprietary IPR.

Mr. Guo was the recipient of the first and second prizes of the National Science and Technology Progress Award in 2008 and 2015, the Ho Leung Ho Lee Foundation Science and Technology Progress Award in 2011 and FEIAP Engineer of the Year Award 2018, in 2019.